

# Pressure anisotropy on twin tunnel linings induced by a transverse gallery construction using time-dependent constitutive models

Bianca M. Girardi<sup>1</sup>, Felipe P. M. Quevedo<sup>1</sup>, Samir Maghous<sup>1</sup>

<sup>1</sup>*Graduate Program in Civil Engineering, Federal University of Rio Grande do Sul  
Av. Osvaldo Aranha, 99, Porto Alegre, 90.035-190, RS, Brazil  
eng.biancagirardi@gmail.com, motta.quevedo@ufrgs.br, samir.maghous@ufrgs.br*

**Abstract.** The increasing construction of twin tunnels demands a comprehensive understanding of their interaction with transverse galleries and the surrounding rock mass. This study conducts a 3D finite element analysis of the junction between deep twin tunnels and a transverse gallery, incorporating time-dependent effects such as rock mass creep, concrete creep, and shrinkage. The model is verified against existing numerical results, confirming its reliability in estimating internal forces in the lining. The influence of different rock mass friction angles on pressure distributions is investigated, revealing that higher friction angles significantly reduce lining pressures, particularly at the end of tunnel construction. The results indicate pronounced anisotropy in pressures, influenced by the properties of the lining and the rock mass, and peak pressures are observed at the lateral sides of the walls. Additionally, viscoelastic linings exhibit increased long-term stress redistribution, emphasizing the role of rheological behavior in tunnel performance. These findings offer valuable insights for the design and reinforcement of tunnel-gallery intersections. The study reinforces the importance of 3D modeling and time-dependent behavior in the safe and accurate design of tunnel-gallery intersections.

**Keywords:** Deep twin tunnels, Transverse gallery, Viscoelastic concrete lining, Elastoplastic-viscoplastic coupled, Finite element model

## 1 Introduction

The increasing demand for underground infrastructure in urban areas has led to a rise in the construction of twin tunnels, typically designed for one-way traffic in each tunnel. For operational and safety purposes, transverse galleries are often incorporated, allowing for interconnections between tunnels. These junction zones represent critical areas in tunnel design due to the complex interactions between the tunnel linings, surrounding rock mass, and construction sequence.

Despite advances in tunneling technology, the interaction mechanisms induced by transverse galleries, especially in deep tunneling scenarios, remain underexplored, mainly due to the computational complexity involved in modeling 3D geometries and sequential excavation processes. The excavation of a transverse gallery causes a redistribution of stresses in the surrounding rock mass, resulting in increased loads on the main tunnel lining near the intersection. When these additional loads exceed the structural capacity of the primary lining, localized instability may occur, raising the risk of failure. Therefore, understanding how deformations and pressures are redistributed in this zone is crucial for the proper design of linings and the placement of structural reinforcements. Incorporating these effects into the design process is essential to ensure the structural integrity and long-term stability of the tunnel system.

The present work extends a previous numerical study by Quevedo et al. [1], providing a detailed three-dimensional finite element analysis of deep twin tunnels connected by a transverse gallery. A coupled elastoplastic-viscoplastic constitutive model is used for the rock mass, while the concrete lining behavior includes viscoelasticity and shrinkage effects. Special attention is given to the anisotropic redistribution of lining pressures in the junction zone, considering different friction angles in the rock mass and comparing elastic and viscoelastic linings.

The results aim to support design decisions by highlighting the importance of using advanced material models and 3D simulations in the analysis of tunnel-gallery intersections, particularly under long-term conditions.

## 2 Constitutive models

The structural response of the tunnel system is governed by time-dependent behaviors in both the concrete lining and the surrounding rock mass.

### 2.1 Concrete lining

The viscoelastic behavior of concrete is modeled using the Solidification Theory developed by Bažant and Prasannan [2, 3], calibrated with the CEB-FIP Model Code 1990 standard specifications formulation CEB-FIP [4] as described in Quevedo et al. [5]. This formulation enables the simulation of delayed deformations and stress redistribution caused by creep and shrinkage in the lining. The creep strain is represented through a Generalized Kelvin chain with aging, while shrinkage is introduced as an isotropic strain field. The stress–strain relationship under infinitesimal strain theory is expressed as:

$$\Delta\sigma = \mathbf{D} : \Delta\epsilon - \mathbf{D} : \Delta\epsilon^{sh} - \mathbf{D}^* : \Delta\epsilon^{cr} \quad (1)$$

where  $\mathbf{D}$  is the elastic constitutive tensor,  $\mathbf{D}^*$  is the same tensor reformulated to account for the viscoelastic effects due to concrete aging, and  $\Delta\epsilon^{sh}$  and  $\Delta\epsilon^{cr}$  are the shrinkage and creep strain increments, respectively.

To match the CEB-FIP MC90 formulation, the parameters of the Bažant-Prasannan model are calibrated through the following equivalences in the creep functions provided by these references:

$$E_0 = E_c(t_0), \quad \gamma(t - t_0) = \beta_c(t - t_0), \quad \frac{1}{v(t)} = \frac{\varphi_0(t_0)}{E_{ci}}, \quad \frac{1}{\eta(t)} \rightarrow 0 \quad (2)$$

In Equation (2),  $t_0$  represents the concrete age at the instant of load application;  $E_c(t_0)$  is the tangent modulus at loading;  $\beta_c(t - t_0)$  is a function of the age of loading  $t - t_0$ ;  $\varphi_0(t_0)$  is the basic creep coefficient;  $E_{ci}$  is the elastic modulus at 28 days;  $v(t)$  is the solidified concrete volume fraction and  $\eta(t)$  is the apparent macroscopic viscosity.

### 2.2 Rock mass

The rock mass is modeled using a coupled elastoplastic-viscoplastic formulation under infinitesimal strain theory. The total strain rate  $\dot{\epsilon}$  is decomposed into elastic  $\dot{\epsilon}^e$ , plastic  $\dot{\epsilon}^p$ , and viscoplastic  $\dot{\epsilon}^{vp}$  components and the constitutive relationships can be written as:

$$\dot{\sigma} = \mathbf{D} : \dot{\epsilon}^e = \mathbf{D} : (\dot{\epsilon} - \dot{\epsilon}^p - \dot{\epsilon}^{vp}) \quad (3)$$

where  $\dot{\sigma}$  is the stress rate,  $\mathbf{D}$  is the elastic constitutive tensor and the inelastic strain rates are given by:

$$\dot{\epsilon}^p = \begin{cases} \lambda^p \frac{\partial f^p}{\partial \sigma}, & \text{for } f^p > 0, \\ 0, & \text{for } f^p \leq 0, \end{cases} \quad \text{and} \quad \dot{\epsilon}^{vp} = \frac{\langle f^{vp} \rangle^n}{\eta} \frac{\partial f^{vp}}{\partial \sigma} \quad (4)$$

In the above relationship,  $\lambda^p$  and  $\lambda^{vp}$  denotes, respectively, the plastic and viscoplastic multiplier,  $f^p$  and  $f^{vp}$  is the plastic and viscoplastic yield function,  $\eta$  is the dynamic viscosity constant (in MPa · day),  $n$  is the dimensionless parameter and  $\langle * \rangle$  is the McCauley function. The short-term behavior is captured using the Drucker–Prager yield criterion:

$$f^p(\sigma, q) = f^p(I_1, J_2, q^p) = \beta_1 I_1 + \beta_2 \sqrt{J_2} - q^p(\alpha^p). \quad (5)$$

This yield surface is inscribed to the Mohr–Coulomb surface and defined in terms of the first invariant of stress tensor  $I_1$ , the second invariant of the deviator tensor  $J_2$ , the parameter related to cohesion  $q^p(\alpha^p)$  and the strength parameters related to the friction angle  $\beta_1$  and  $\beta_2$ . These terms are given by Bernaud [6]:

$$\beta_1 = \frac{(k^p - 1)}{3}, \beta_2 = \frac{(2k^p + 1)}{\sqrt{3}}, q^p(\alpha^p) = 2\sqrt{k^p} c^p(\alpha^p), \quad (6)$$

where  $k^P = (1 + \sin \phi^P)/(1 - \sin \phi^P)$  and  $\alpha^P$  is the internal variable associated with the hardening and softening of the material.

Consistent with the elastoplastic approach, the viscoplastic yield function also adopts the Drucker–Prager yield criterion. As a consequence, the coefficients  $\beta_1$  and  $\beta_2$  of eq. (6) are evaluated by replacing  $k^P$  for  $k^{vP} = (1 + \sin \phi^{vP})/(1 - \sin \phi^{vP})$ . Also, the viscoplastic cohesion parameter then becomes  $q^{vP} = 2\sqrt{k^{vP}}c^{vP}(\alpha^{vP})$ . In this study, both plastic and viscous flow rules are implemented with associative potentials, assuming perfect plasticity and viscoplasticity (i. e., cohesions  $c^P$  and  $c^{vP}$  assumed to remain constant).

### 3 Spatial and time discretization of the domain

The finite element simulations were performed using a three-dimensional model representing deep twin tunnels connected by a transverse gallery. The geometry was reduced by symmetry, modeling only one-quarter of the domain, represented as  $\Omega$  (see Fig. 1). The analysis assumes deep tunnel conditions ( $H \gg R_t$ ), with  $H$  being the overburden depth and  $R_t$  the longitudinal tunnel radius and the transverse gallery radius  $R_g$  is smaller than  $R_t$  ( $R_g < R_t$ ). Referring to the notations of Fig. 1,  $d_1$  is the distance between the axes of longitudinal tunnels and  $d_2$  characterizes the location of the transverse axis gallery intersects the longitudinal tunnel.

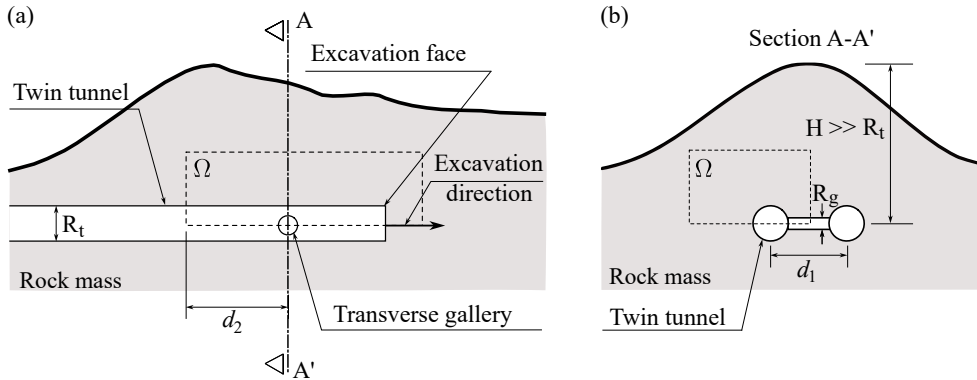


Figure 1. Schematic representation of the twin tunnels geometry problem: (a) longitudinal view and (b) section A-A'.

The computational domain consists of a parallelepiped volume with dimensions  $(L_1 + L_2) \times L_3 \times d_3$ , as presented in Fig. 2. Symmetry conditions are imposed on the planes  $x = 0$ ,  $y = 0$ , and  $z = L_1 + L_2$ , reducing the computational cost of the analysis. This approach assumes that the longitudinal tunnels are excavated synchronously and the transverse gallery is excavated from the tunnels towards the center. Initial isotropic in-situ geostatic stresses are applied with vertical  $\sigma_v$  and horizontal  $\sigma_h$  constant stresses. The boundary pressures are  $-\sigma_v$  at the upper plane  $y = d_3$  and  $-\sigma_h$  at the left-lateral  $x = -L_3$  and back  $z = 0$  planes.

Discretization is performed using 8-node trilinear hexahedral elements with full integration. In regions with complex geometry, such as the tunnel-gallery intersection, 8-node linear tetrahedral elements are used. A refined mesh is employed in the zones near the longitudinal tunnel, indicated by light gray color in Fig. 2 and tunnel-gallery junction zone (see details in Fig. 3) to ensure accuracy in stress and deformation fields. The total mesh consists of approximately 617,000 elements.

The geometric and construction parameters adopted in the analysis define the radius of the longitudinal tunnels as  $R_t$ , while the radius of the gallery is set to  $R_g = 0.5R_t$ . The thickness of the concrete lining is the same for both the longitudinal tunnels and the gallery, given by  $e_t = e_g = 0.05R_t$ . Also, the distance between longitudinal tunnel axes is denoted by  $d_1 = 4R_t$ .

The excavation process is modeled using an activation–deactivation technique. The longitudinal tunnel excavation is simulated by deactivating solid elements (reducing their stiffness), followed by activation of lining elements at a specified distance from the face (unlined distance  $d_{0t} = 2R_t/3$ ). Each excavation step ( $L_{pt} = R_t/3$ ) is associated with a time interval  $t_p = L_{pt}/V_{pt}$ , where  $V_{pt} = 12.5$  m/day is the excavation speed. The gallery is excavated after complete a predefined number of steps ( $n_{pig} = 15$ ) beyond the  $d_2$  distance in the longitudinal tunnel and follows the same procedure with  $L_{pg} = 0.2R_g$ ,  $V_{pg} = 12.5$  m/day and  $d_{0g}$ .

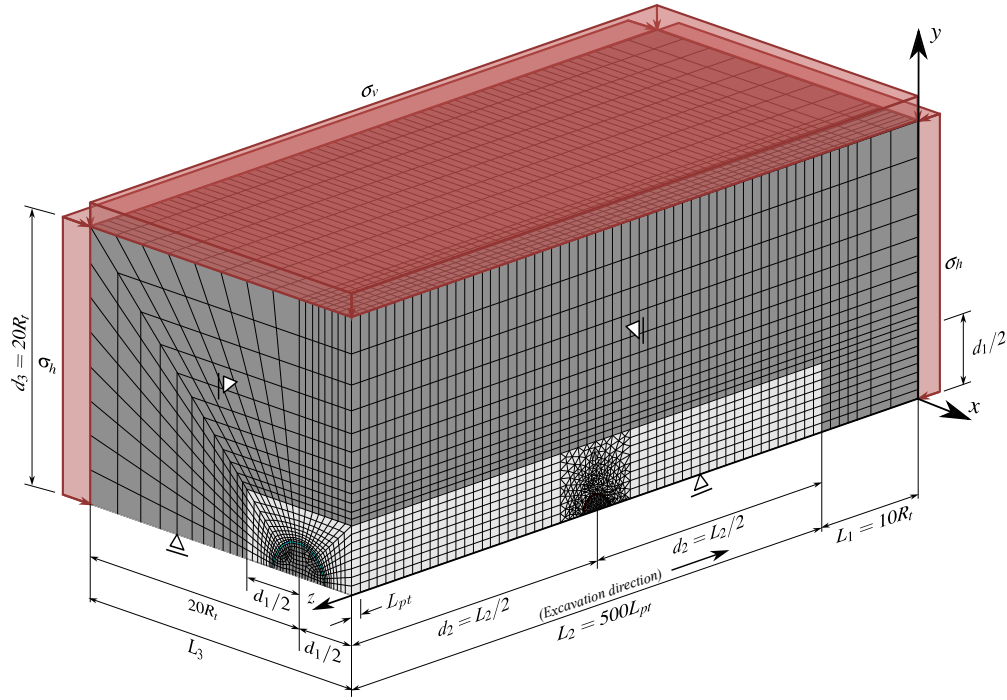
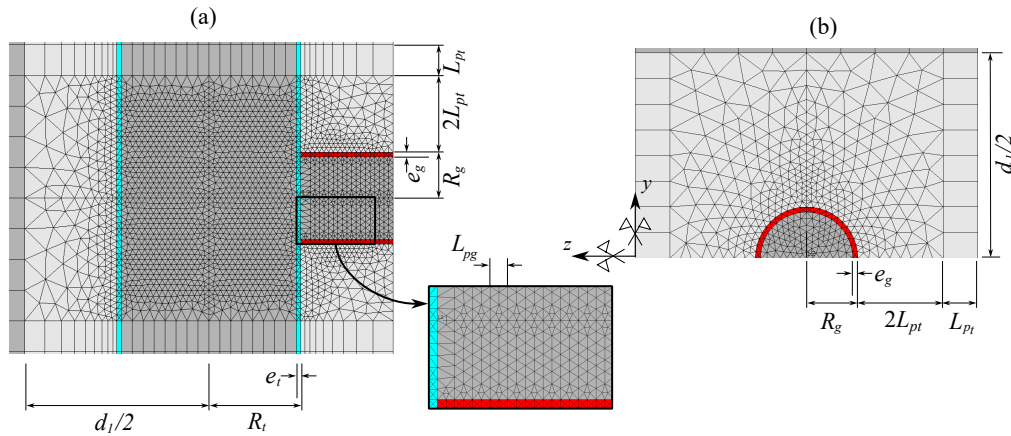


Figure 2. Mesh, dimensions and boundary conditions of the twin tunnels with gallery domain.


 Figure 3. Geometry and F. E mesh: (a) longitudinal tunnel and gallery in the symmetry plane  $y = 0$  and (b) gallery cross-section

## 4 Computational model verification

This section aims to verify the computational model's capability to simulate circumferential internal forces induced in the tunnel lining by the transverse gallery construction. For this verification, results from 3D finite element analyses by Chortis and Kavvas [7] are compared with those obtained from the present F.E. model.

Chortis and Kavvas [7] modeled the rock mass using solid elements and a linear elastic perfect plastic behavior based on the Generalized Hoek-Brown criterion. The shotcrete lining was represented by shell elements with linear elastic properties. In the present study, the Hoek-Brown criterion was approximated by the Mohr-Coulomb model using the formulation proposed by Hoek et al. [8], obtaining yielding cohesion and friction angle values of 0.14 MPa and  $28.72^\circ$ , respectively, for implementation in the numerical model.

While Chortis and Kavvas [7] explored a range of geometric and constitutive parameters through parametric analyses, in this study were adopted fixed values for these parameters: radius ratio between the longitudinal tunnel and the gallery  $R_t/R_g = 1.33$ , distance between longitudinal tunnel axes  $d_1 = 8R_t$ , overburden height  $H = 80$  m, isotropic initial stress  $\sigma_v = \sigma_h = 2$  MPa, rock mass Young modulus  $E_m = 562$  MPa and Poisson ratio  $\nu_m = 0.3$ ,

shotcrete Young modulus  $E_{c28} = 20$  GPa and Poisson ratio  $\nu_c = 0.2$ . The internal forces in the tunnel lining were evaluated at the end of construction using a normalized circumferential  $N_C^* = N_C / (p_0 D)$  component and are presented in Figure 4 at a normalized distance  $S/D$ , where  $S$  is the distance from the gallery axis and  $D$  is the diameter of the main tunnel.

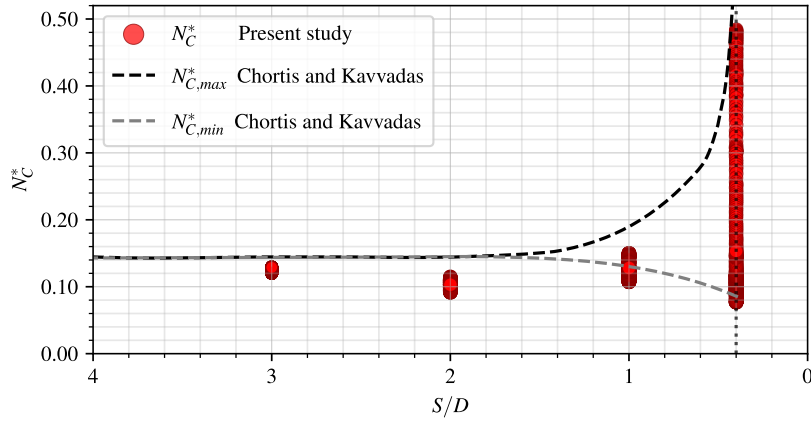


Figure 4. Normalized circumferential internal force on the main tunnel at the end of construction.

In Figure 4, results near the transverse gallery were consistent with those reported by Chortis and Kavvadas [7], confirming the concentration of effects in that region. Further from the gallery, lower values were observed, likely due to differences in modeling strategies, including element types, excavation procedures, and constitutive criteria.

## 5 Three-dimensional finite element simulations

This section presents numerical results related to the anisotropy of pressures in the twin tunnel walls in the intersection gallery-tunnel zone, considering both elastic (EL) and viscoelastic (VEL) lining behaviors. The rock mass was modeled with an elastic modulus  $E_m = 1400$  MPa and Poisson's ratio  $\nu_m = 0.4$ . The Drucker–Prager plasticity model was adopted with cohesion  $c^p = 4$  MPa and friction angles  $\phi^p = 0^\circ$  and  $5^\circ$ . Viscoplastic behavior was incorporated using a viscosity coefficient  $\eta = 40,000$  MPa · day, viscoplastic cohesion  $c^{vp} = 2$  MPa, and viscoplastic friction angle  $\phi^{vp} = 0^\circ$ . For the concrete lining, the 28-day elastic modulus was  $E_{c28} = 25,146$  MPa and Poisson's ratio  $\nu_c = 0.2$ .

Numerical results of lining pressures are presented at the end of construction and after 3,000 days, representing long-term viscous stabilization. The anisotropies of pressures are represented by:

$$\chi(\theta) = \frac{p(\theta)}{p(\theta = 90^\circ)}, \quad (7)$$

where  $\theta$  denotes the cylindrical angle along the tunnel wall perimeter and  $p(\theta)$  represents the pressure on the longitudinal tunnel lining. The results are normalized by the pressure at  $\theta = 90^\circ$ , which corresponds to the reference value of the crown in main tunnel. Two sections, S1 and S2, were adopted along the longitudinal tunnel and their locations are shown in Fig. 5. Section S2 is located at the centerline of the transverse gallery, while S1 is positioned at a distance of  $4R_g/3$  along the  $z$ -axis. No results are available for  $0^\circ < \theta < 30^\circ$  in S2, as this region corresponds to the gallery entrance. Figure 6 shows the anisotropy results at the end of construction, with elastic (a) and viscoelastic (b) linings, and in the long-term with elastic (c) and viscoelastic (d) linings.

Figure 6 shows that the lining pressures remain close to the reference value  $p(\theta)$ , except in the range  $0^\circ < \theta < 60^\circ$ , where a significantly increase is observed, reaching about twice the crown pressure in S1 at  $\theta = 0^\circ$  with higher anisotropy value in the end of construction with viscoelastic lining.

The friction angle influences pressure distribution, especially in section S2 at  $30^\circ < \theta < 90^\circ$ , where higher angles reduce pressures above the gallery entrance and amplify the contrast with the crown, reflecting greater rock mass support and lower stress transfer to the lining. Regarding the reference pressure  $p(90^\circ)$ , higher values are observed in section S2 compared to section S1, about 14% for  $\phi = 0^\circ$  in both elastic and viscoelastic linings,

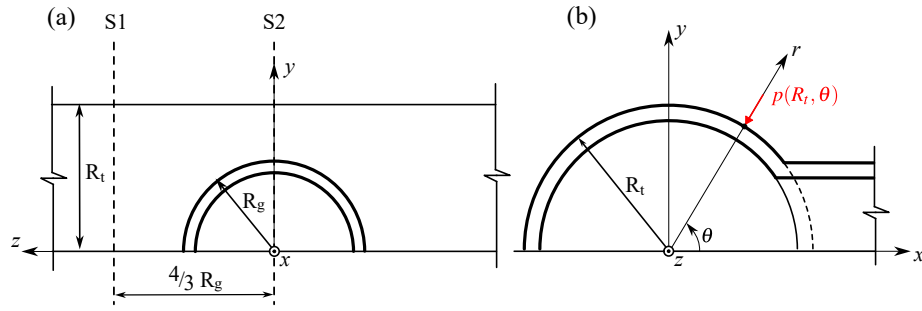


Figure 5. (a) Schematic representation of the sections S1 and S2 in the longitudinal tunnel, (b) S2 and representation of pressure on the lining.

indicating that the construction of the transverse gallery significantly affects the redistribution of stresses along the tunnel at the end of construction.

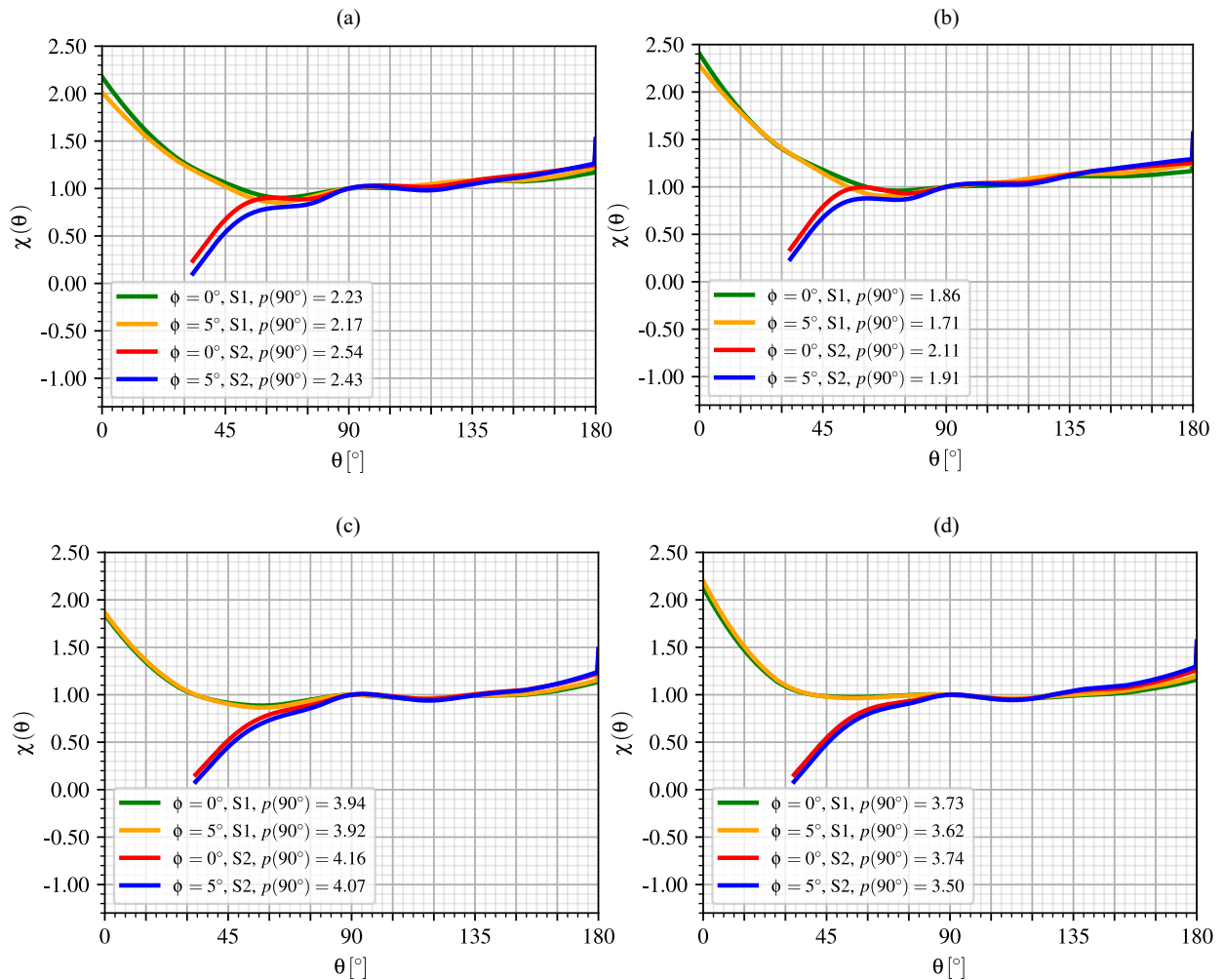


Figure 6. Anisotropy of pressures in longitudinal tunnel lining at the end of construction with (a) elastic lining and (b) viscoelastic lining and at the long-term with (c) elastic lining and (d) viscoelastic lining.

The long-term pressures presented in ?? have a similar behavior to the end of construction but with increased magnitudes, and the influence of the friction angle is less pronounced. Overall, stress concentrations tend to be higher at the lateral sides of the tunnels ( $\theta = 0^\circ$  and  $180^\circ$ ).

In the case of elastic lining, the highest crown pressure occurs in section S2, although the increase compared

to section S1 at the end of construction is relatively lower, around 6% for a friction angle of  $\phi = 0^\circ$ . In contrast, with a viscoelastic lining, the crown pressure remains nearly identical between the two sections for  $\phi = 0^\circ$ , and even decreases by approximately 4% in section S2 when  $\phi = 5^\circ$ .

## 6 Conclusions

The computational model verification confirmed its accuracy in capturing internal forces in tunnel linings, particularly near the transverse gallery where interactions are more significant. Discrepancies in regions farther from the gallery are mainly due to differences in modeling approaches, including element types, excavation methods, and constitutive criteria.

The results obtained demonstrate the impact of constructing the transverse gallery on the redistribution of pressures along the lining of the twin tunnels. It can be observed that, at the end of construction, there is a significant increase in pressure in the lining in the lateral region adjacent to the parallel tunnel, especially in section S2, which is located on the axis of the gallery. This behavior indicates that the excavation of the transversal gallery generates a concentration of stresses above its entrance, altering the distribution. The greater angle of friction contributed to a decrease in pressures in this region.

In the long term, the pressures increase in magnitude, but the influence of the friction angle becomes less significant. Nevertheless, it is possible to observe relevant differences between the types of lining. The viscoelastic lining shows greater anisotropy in relation to the crown at  $\phi = 0^\circ$  when compared to elastic concrete. These results underscore the importance of considering the time-dependent behavior of materials and the properties of the rock mass during the design stage, particularly in critical areas such as the intersection between tunnels and galleries.

Overall, the results highlight the importance of using advanced material models and 3D analyses for the safe and realistic design of complex underground structures, especially in deep twin tunnel-gallery junctions with long-term and interactions conditions.

**Acknowledgements.** The authors gratefully appreciate the provided by the Brazilian Research (CNPq) and the Brazilian Federal Agency for Support Evaluation of Graduate Education (CAPES).

**Authorship statement.** The authors hereby confirm that they are the sole liable persons responsible for the authorship of this work, and that all material that has been herein included as part of the present paper is either the property (and authorship) of the authors, or has the permission of the owners to be included here.

## References

- [1] F. P. M. Quevedo, C. A. M. M. Colombo, D. Bernaud, and S. Maghous. 3d finite element analysis of rock deformation in twin circular tunnels with a transverse gallery using plasticity and time-dependent models. *Geotechnical and Geological Engineering*, vol. 1, n. 149, pp. 1–33, 202.
- [2] Z. P. Bažant and S. Prasannan. Solidification theory for concrete creep. I: Formulation. *Journal of Engineering Mechanics*, vol. 115, n. 8, pp. 1691–1703, 1989a.
- [3] Z. P. Bažant and S. Prasannan. Solidification theory for concrete creep. II: Verification and application. *Journal of Engineering Mechanics*, vol. 115, n. 8, pp. 1704–1725, 1989b.
- [4] CEB-FIP. *CEB-FIP model code 1990: Design code*. Comité Euro International du Béton and Fédération Internationale de la Précontrainte (CEB-FIP), 1993.
- [5] F. P. M. Quevedo, R. J. Schmitz, I. B. Morsch, C. F. A., and D. Bernaud. Customization of a software of finite elements to analysis of concrete structures: long-term effects. *IBRACON Structures and Materials Journal*, vol. 11, n. 4, pp. 696–718, 2018.
- [6] D. Bernaud. *Tunnels profonds dans les milieux viscoplastiques: approches expérimentale et numérique*. Ph.D. Thesis (in french), Ecole Nationale des Ponts et Chaussées, Paris, France, 1991.
- [7] F. Chortis and M. Kavvas. 3d numerical investigation of the axial forces acting on tunnel junctions constructed in fractured/weathered to very blocky rockmass. *Expanding Underground - Knowledge and Passion to Make a Positive Impact on the World*, pp. 1574–1582, 2023.
- [8] E. Hoek, C. Carranza-Torres, and B. Corkum. Hoek-brown failure criterion 2002 edition. *Proceedings of the North American Rock Mechanics Society Meeting*, pp. 267–273, 2002.